actuators

MDPI

Article

Fast Electrical Activation of Shape Memory Alloy Spring Actuators: Sub-Second Response Characterization and Performance Optimization

Stefano Rodinò [1,2,*], Matteo Chiodo [2], Antonio Corigliano [2], Giuseppe Rota [2] and Carmine Maletta [1,2]

[1] DIMEG (Department of Mechanical, Energy and Management Engineering), University of Calabria—UNICAL, Via Ponte Pietro Bucci 44C, Rende, 87036 Cosenza, Italy; carmine.maletta@unical.it
[2] 2SMArtEST, Via Ponte Pietro Bucci 44C, Rende, 87036 Cosenza, Italy; matteo.chiodo@2smartest.com (M.C.); antonio.corigliano@2smartest.com (A.C.); giuseppe.rota@2smartest.com (G.R.)
* Correspondence: stefano.rodino@unical.it

Abstract

Background: Shape memory alloy spring actuators offer significant potential for advanced actuation systems in exoskeletons, medical devices, and robotics, but adoption has been limited by slow activation speeds and insufficient design guidelines for achieving rapid response times while maintaining structural integrity. Objective: This study aimed to establish comprehensive design parameters for nickel–titanium spring actuators capable of achieving sub-second activation times through systematic experimental characterization and performance optimization. Methods: Nine different nickel–titanium spring configurations with wire diameters ranging from 0.5 to 0.8 mm and spring indices from 6 to 8 were systematically evaluated using differential scanning calorimetry for thermal characterization, mechanical testing for material properties, high-current electrical activation studies spanning 5–11 A, infrared thermal distribution analysis, and laser displacement sensing for dynamic response measurement. Results: Dynamic testing achieved activation times below 1 s for currents exceeding 5 A, with maximum displacement recoveries reaching 600–800% strain recovery, while springs with intermediate spring index values of 6.5–7.5 provided optimal balance between force output and displacement range, and optimal activation involved moderate current levels of 5–7 A for thin wires and 8–11 A for thick wires. Conclusions: Systematic geometric optimization combined with controlled high-current density activation protocols enables rapid actuation response while maintaining structural integrity, providing essential design parameters for engineering applications requiring fast, reliable actuation cycles.

Keywords: shape memory alloy; fast actuation; electrothermal activation; spring actuators; sub-second response; thermomechanical characterization; dynamic performance optimization; NiTi alloys

check for updates

Academic Editors: Maria Dolores Blanco Rojas, Dorin Sabin Copaci and Janeth Ileana Arias Guadalupe

Received: 2 October 2025
Revised: 10 November 2025
Accepted: 11 November 2025
Published: 2 December 2025

Citation: Rodinò, S.; Chiodo, M.; Corigliano, A.; Rota, G.; Maletta, C. Fast Electrical Activation of Shape Memory Alloy Spring Actuators: Sub-Second Response Characterization and Performance Optimization. *Actuators* **2025**, *14*, 584. https://doi.org/10.3390/act14120584

Copyright: © 2025 by the authors. Licensee MDPI, Basel, Switzerland. This article is an open access article distributed under the terms and conditions of the Creative Commons Attribution (CC BY) license (https://creativecommons.org/licenses/by/4.0/).

1. Introduction

Shape memory alloys (SMAs) represent a transformative class of materials for smart actuator applications, distinguished by their capacity to return to predefined configurations through thermal stimulus while producing significant forces and displacements in miniaturized designs [1,2]. This performance advantage positions them favorably against comparable smart actuator technologies such as thermally driven artificial muscles (TCAMs) [3]. Among various SMA configurations, helical springs represent one of the most practical and

efficient geometries for actuation applications, combining the shape memory effect with the mechanical advantage of spring geometry to create actuators capable of addressing demanding engineering requirements across multiple technological sectors [4,5]. The development of SMA spring actuators for advanced applications requires a comprehensive understanding of their static and dynamic characteristics governed by solid-state phase transformations between the crystal structures of austenite and martensite [6]. The driving force governing the reorganization of martensitic variants is the free energy difference across the twin boundaries [7]. This transformation behavior is highly dependent on material composition, thermal treatment, mechanical loading, and geometric configuration [8,9]. Unlike conventional actuators, SMA springs exhibit complex thermomechanical behavior involving multiple interconnected variables including wire diameter, coil diameter, number of turns, spring index, and material composition, each significantly influencing the actuator's force output, displacement range, response time, and operational reliability [10–12]. Recent advances in SMA technology have focused on optimizing actuator performance through careful control of material properties and geometric parameters [13,14]. Practical applications demonstrate transformative potential across industries, with SMA actuators achieving remarkable performance metrics. In assistive devices and prosthetics, anthropomorphic prosthetic hands have achieved up to 20 degrees of freedom and human-like grasping capabilities, with performance metrics including 0.5 kg weight for full five-finger prosthetic hands, 0.3 s response times for 100 μm diameter SMA wires, and up to 0.8 N tip force per finger [15,16]. Biomedical and rehabilitation applications take advantage of the unique properties of SMA for magnetic resonance imaging (MRI)-compatible systems, neurosurgical robots, and ankle rehabilitation platforms, benefitting from excellent biocompatibility, corrosion resistance, and tissue compatibility [17,18]. Exoskeletons and wearable systems have advanced to pediatric applications, with SMA-actuated systems supporting cerebral palsy rehabilitation in 8-year-old patients [19]. Recent applications include the use of magnetic shape memory alloys (MSMAs) for magnetic field sensors by coupling them with optical fibers [20]. Manufacturing advances have enabled unprecedented design flexibility. Recent developments in 3D printing integration enable entire multi-articulated hands to be manufactured without assembly and a morphable surface for aerodynamic applications [21], while 4D printing applications create shape-morphing structures with programmable actuation capabilities [22]. These manufacturing advances significantly reduce production costs and enable complex geometries that were previously impossible with traditional fabrication methods. Current research challenges in SMA spring actuator development include predicting performance characteristics during the design phase, optimizing thermal activation. The non-linear behavior of SMAs, characterized by complex interactions between thermal, electrical, and mechanical fields, presents significant challenges in the design phase, rendering it inherently iterative and computationally intensive. The multifaceted nature of these materials, with their strong dependence on geometric variables and operating conditions, coupled with intricate electro-thermo-mechanical interactions, necessitates comprehensive experimental characterization to establish reliable design guidelines and validatex computational models [23]. This complex behavioral framework requires systematic investigation across multiple physical domains to develop robust design methodologies capable of predicting material performance under diverse operational scenarios. Issues such as fatigue, performance degradation after repeated cycles, and difficulty in achieving precise and accurate control due to the thermal nature of activation are critical aspects that must be addressed [24,25]. To overcome the intrinsic hysteresis that limits actuator accuracy, control strategies based on neural networks and iterative learning have been developed [26].

Despite significant theoretical advances, a substantial gap persists between sophisticated theoretical modeling capabilities and practical design tools suitable for engineering applications. Most existing approaches require extensive computational resources and specialized expertise, limiting their adoption in industrial settings [27,28]. Recent developments in multiphysics modeling have attempted to address these limitations through comprehensive 1D coupled-field simulations [29,30]. The lack of standardized evaluation methodologies for SMA actuators further complicates the systematic comparison of performance across different studies and applications [31], highlighting the critical need for simplified yet accurate design frameworks that bridge the gap between theoretical rigor and practical implementation. Extensive computational frameworks have been developed to address SMA actuator complexity, including energy-balance simulation tools [32], electro-thermo-mechanical formulations for stress-dependent behavior [33], and predictive models for activation dynamics incorporating material variability [14]. However, these approaches inadequately capture dynamic effects under high-current electrical activation [34,35], particularly the rapid thermal transients that generate stress levels exceeding 1.8 GPa and strain rates of 10^3 s^{-1}. Fast actuation strategies have emerged as transformative approaches for SMA performance enhancement. Motzki et al. [36] demonstrated energy-efficient millisecond-pulse activation achieving 4% stroke recovery with 80% energy savings compared to conventional activation methods. Comprehensive analytical frameworks for high-rate actuation [37] have established design guidelines for enhanced energy efficiency and reduced response times, yet practical implementation remains constrained by computational complexity and limited experimental validation across diverse geometric configurations. Advanced thermal management represents a critical frontier in SMA actuator development, with recent investigations achieving unprecedented energy efficiency through innovative activation strategies. Zhang et al. [38] developed comprehensive numerical models capable of simulating dynamic effects, systematically examining actuation responses of biased NiTi SMA wire actuators under varying electric heating rates and 40~MPa applied static stress, revealing complex dynamic responses during high heating current pulse actuation. Thermal management breakthroughs have demonstrated transformative energy efficiency improvements in SMA actuators. High-voltage pulse activation represents a paradigm shift, achieving 60–80% energy savings compared to conventional control methods [36]. This adiabatic activation approach employs rapid heating pulses (12 V for 0.1 ms versus conventional 3 V for 5 s) to minimize heat loss to the environment, enabling rapid actuation while dramatically reducing power consumption through optimized energy transfer mechanisms. Systematic experimental evaluation of SMA wire actuators under controlled electrical heating protocols has demonstrated sub-200 ms activation capabilities, establishing critical design parameters for high-speed thermomechanical response [29]. Advanced cooling techniques have evolved beyond simple convective approaches. Liquid-jet cooling studies demonstrate improved heat transfer coefficients for moving SMA surfaces, while forced convection systems significantly reduce deactivation time and create symmetric activation profiles [39]. Novel approaches include grease-filled PTFE tubes showing 25% cooling time reduction and carbon nanotube coating providing uniform heat distribution with improved thermal stability [40]. Inductive heating has gained prominence as a contactless activation method using electromagnetic fields at 10^4–10^6 Hz frequencies, producing more linear stress–strain characteristics compared to direct heating [41]. This study addresses fundamental limitations in contemporary SMA actuator technology through systematic experimental investigation of nine different SMA spring configurations manufactured from NiTi alloys with varying geometric parameters. Wire diameters ranging from 0.5 to 0.8 mm and spring indices from 6.0 to 8.5 were systematically evaluated to establish comprehensive design guidelines that address

critical knowledge gaps in the current literature. Existing SMA spring characterization studies, predominantly conducted between 2002 and 2004 [42–44], demonstrate significant methodological constraints when evaluated against current technological demands. Previous investigations were fundamentally limited by narrow current density exploration (maximum 8.4–12.2 A/mm^2), single-parameter focus without systematic optimization, and simplified experimental protocols employing basic measurement techniques. These foundational studies inadequately address contemporary requirements for high-speed actuation systems operating under extreme conditions. This investigation systematically addresses these limitations through comprehensive high-current density characterization extending experimental exploration to unprecedented levels reaching 56 A/mm^2, representing a 560% increase over maximum values reported in the foundational literature. This substantial extension enables investigation of rapid activation phenomena, thermal distribution effects, and performance optimization strategies previously inaccessible to historical research constrained by instrumentation limitations. The research objectives focus on systematic high-current density evaluation through four integrated experimental domains: (1) comprehensive thermal characterization using differential scanning calorimetry to establish baseline transformation temperatures across geometric configurations, (2) mechanical property determination through quasi-static testing to extract fundamental material parameters, (3) extensive dynamic response analysis under controlled high-current electrical activation spanning 5–56 A/mm^2 to evaluate activation times and displacement capabilities, and (4) comprehensive performance mapping for engineering design applications. Results demonstrate that systematic geometric optimization combined with controlled high-current density activation protocols enable rapid actuation response while maintaining structural integrity. Dynamic testing revealed activation times below 1 s for currents exceeding 5 A, with progressive performance enhancement across the complete current density range extending to 56 A/mm^2. Maximum displacements reaching 600–800% strain recovery establish new performance benchmarks while providing validated design data across previously unexplored operational regimes. The findings provide essential design parameters for SMA spring actuator optimization in applications requiring fast, reliable actuation cycles across robotics, aerospace, biomedical, and automation sectors. This research addresses critical knowledge gaps in rapid electrical activation of SMA spring actuators through comprehensive experimental investigation and systematic design space exploration. The principal contributions of this work include the following: (1) comprehensive parametric mapping of fast actuation characteristics (t_a < 2 s) across extensive geometric design space exceeding previous studies' activation electric current density; (2) development of validated analytical–experimental framework for rapid design iteration; (3) generation of performance maps enabling direct selection of optimal actuation parameters; (4) establishment of design guidelines for high-frequency cyclic operation in robotic applications. Unlike previous studies focusing on individual spring geometries or steady-state behavior, this work provides a systematic methodology for actuator selection and optimization applicable across diverse engineering applications.

This paper is organized as follows: Section 2 presents the materials and methods, including the characterization of nine NiTi spring configurations through differential scanning calorimetry, mechanical testing, and dynamic activation studies using infrared thermography and laser displacement sensors. Section 3 reports the results and discussion, covering static behavior under constant stress recovery, dynamic performance analysis demonstrating sub-second activation times, and systematic evaluation of geometric parameter influences on actuator performance. The experimental findings are validated against a simplified mathematical model combining spring mechanics with SMA constitutive behavior. Performance optimization guidelines are established for wire diameter selection,

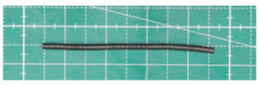
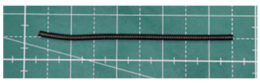
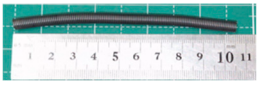
spring index optimization, and thermal management strategies. This study concludes with practical design parameters for engineering applications requiring fast, reliable SMA spring actuation cycles.

2. Materials and Methods

2.1. SMA Springs' Geometry and Material

Nine different SMA spring configurations were manufactured from NiTi alloy wire, supplied by commercial vendors Xian Zhanwo Metal Material Co., Ltd. (Xi'an, China). The material used in this investigation is a commercial Ti-rich NiTi-based SMA wire, with Ti at 51%. The springs were designated as Types 1–9 with varying geometric parameters as detailed in Table 1. Wire diameters, d, ranged from 0.5 mm to 0.8 mm, representing the most common sizes for small-scale actuation applications. The external diameters, D_{ext}, varied from 3 to 6 mm, while the spring indices ($C = D_{ext}/d$) [45] ranged from 6.0 to 8.

Table 1. Geometric parameters of the tested SMA springs.

Spring	D_{ext} [mm]	D_{int} [mm]	d [mm]	Length [mm]	Spring Index	Image
1	4.0 *	3.0	0.5	105	8.00	
2	3.0	2.0	0.5	105	6.00	
3	4.0	2.8	0.6	102	6.67	
4	4.0	2.7	0.65	103	6.15	
5	5.5	4.1	0.7	104	7.86	
6	5.0	3.6	0.7	104	7.14	
7	4.5	3.1	0.7	103	6.43	
8	6.0	4.4	0.8	110	7.50	
9	5.0	3.4	0.8	102	6.25	

* All dimensions are nominal dimensions, provided by the manufacturer; initial coil pitch angle (α_i) is considered 0 for all springs.

Differential Scanning Calorimetry (DSC) analysis was performed using a TA Instruments (New Castle, DE, USA) Waters Discovery DSC 25 DSC machine to determine transformation temperatures for each spring configuration. Small wire samples (5–10 mg) were extracted from representative springs and analyzed using a high-precision DSC system with temperature scanning rates of 10 °C/min. Both heating and cooling cycles were performed over the temperature range of −75 °C to +120 °C to capture complete transfor-

mation behavior. Transformation temperatures were determined using the tangent method at peak onset and finish points. The following parameters were extracted: martensite start (M_s), martensite finish (M_f), austenite start (A_s), and austenite finish (A_f) temperatures as reported in Figure 1a. Mechanical characterization was performed using an MTS Criterion Model 42 electromechanical test system. It revealed the expected nonlinear stress–strain behavior characteristic of shape memory alloy materials under controlled quasi-static loading conditions. Table 2 summarizes the key mechanical properties extracted from experimental data, obtained by following the procedure proposed in [45].

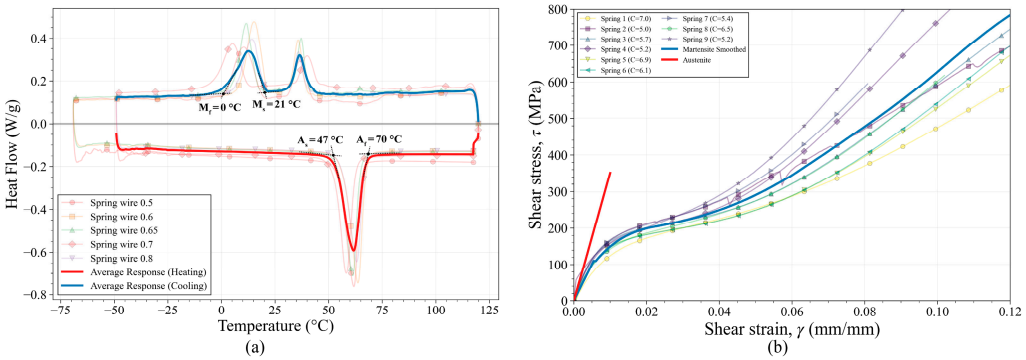


Figure 1. (**a**) DSC analysis: spring wire comparison with average response, (**b**) Stress–strain curves with individual spring legends with average response.

Table 2. Mechanical properties of NiTi shape memory alloy springs.

Spring Type	G_A [MPa]	G_M [MPa]	γ_L	Spring Index (C)
1	39.0	14.0	0.043	8.00
2	31.0	15.0	0.040	6.00
3	36.0	15.0	0.044	6.67
4	35.0	22.0	0.040	6.15
5	32.0	17.0	0.047	7.86
6	37.0	22.0	0.046	7.14
7	30.0	24.0	0.043	6.43
8	35.0	24.0	0.044	7.50
9	32.0	26.0	0.044	6.25
Average	**32.1**	**19.6**	**0.0434**	**6.89**

The stress–strain relationships for all spring configurations (Figure 1b) clearly demonstrate the characteristic detwinning behavior of SMA materials under controlled quasi-static loading conditions with strain rates maintained at 10^{-4} s^{-1} to ensure isothermal test conditions and minimize rate-dependent effects. The austenite and martensite regions are distinctly identifiable, with critical stress levels ranging from 100 to 250 MPa depending on spring geometry and loading rate sensitivity. The austenite shear modulus (G_A) values ranged from 30.0 to 39.0 GPa, averaging 32.1 $\pm$ 7.8 GPa, while martensite modulus (G_M) values were consistently lower, ranging from 14.0 to 26.0 GPa with an average of 19.6 $\pm$ 4.3 GPa. This modulus ratio ($G_A/G_M \approx 1.64$) is characteristic of NiTi alloys and reflects the different crystal structure stiffnesses. Springs with smaller wire diameters (0.5–0.6 mm) exhibit higher critical stress due to increased constraint effects, while larger diameter springs (0.7–0.8 mm) show more gradual detwinning transitions. The measured shear moduli agree well with the established literature values for NiTi alloys [45]. Maximum recoverable shear strain (γ_L) values were remarkably consistent across all spring types, averaging 0.0434 $\pm$ 0.0024. The stress–strain curves exhibited the characteristic

three-stage behavior: initial elastic loading, martensite detwinning plateau, and final elastic loading of detwinned martensite.

2.2. Fast Activation: Experimental Design and Methodology

2.2.1. Advanced Characterization Setup and Instrumentation

A custom experimental setup was designed and constructed for comprehensive mechanical and thermal characterization of SMA springs under quasi-static and fast recovery tests. The system consisted of a rigid vertical frame with precision linear guides, calibrated weights for constant force application, and advanced sensing instrumentation for displacement and temperature monitoring. Key components of the experimental setup included:

1. High-precision load cell (HBM (Milano, Italy) U9C, 1kN capacity) for force measurement;
2. Non-contact laser displacement sensor (Micro-Epsilon (Porto Mantovano, Italy) optoNCDT-1220) with micrometer resolution;
3. Infrared thermal camera (Teledyne FLIR (Wilsonville, OR, USA) A615) for real-time temperature monitoring;
4. Programmable power supply (Aim-TTi (Huntingdon, UK) CPX400DP) for controlled electrical activation;
5. Data acquisition system (HBM (Milano, Italy) QuantumX 840A) for synchronized data collection.

The vertical constraint system (Figure 2) ensured purely axial loading while eliminating lateral displacements that could affect measurement accuracy. All sensors were calibrated prior to testing using certified reference standards.

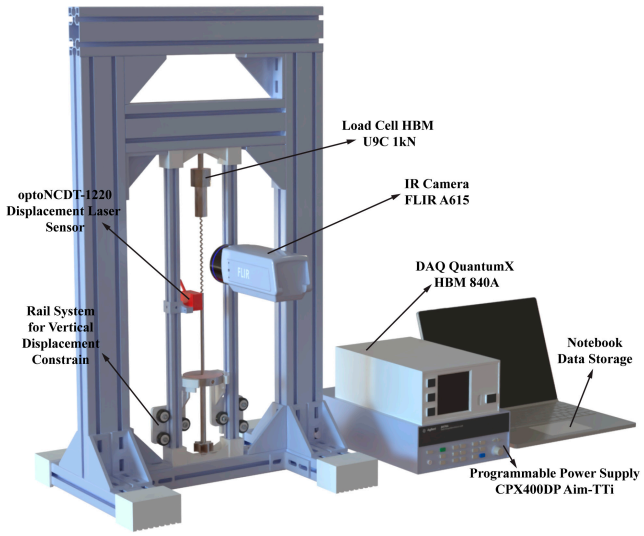


Figure 2. Experimental setup configuration for SMA spring characterization.

2.2.2. Systematic Stress Level Selection Framework

The analytical framework presented in Equations (1)–(11) is directly adapted from the simplified model proposed by An et al. [45], which we gratefully acknowledge. Their approach provides a computationally efficient method for first-order estimation of SMA spring behavior. We extend their methodology by integrating it with classical spring mechanics [46] and applying it systematically across a broad design space of spring geometries and loading conditions. It is important to note that, while this method provides a reasonably accurate first-order estimation aligned with the intended objectives, it remains an approximate model. As such, the results deviate from experimental data to varying degrees depending on the specific segment of the response under consideration.

For the implementation of the simplified model, the geometric parameters of the spring are defined, including its length L, wire diameter d, coil diameter D, the inclination angle of the coil α, and n number of coils. The parameters are illustrated in Figure 3.

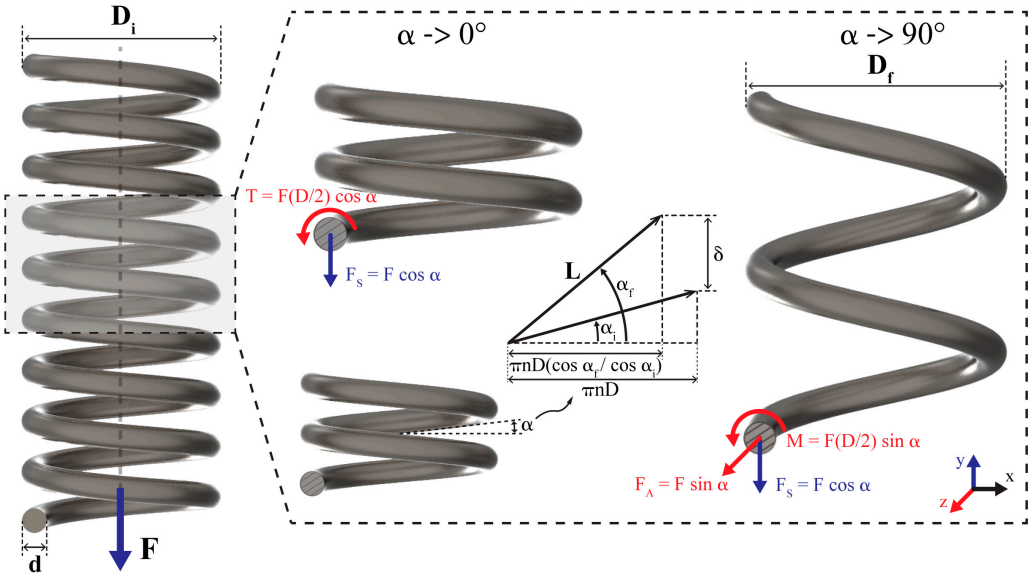


Figure 3. Geometric parametrization and kinematic analysis of helical SMA springs for simplified design model implementation.

The inclination angle of the coil α, an important parameter in the context of the implemented model, can be extracted from the pitch of the coil p and its external diameter. As the pitch is comparable to the wire diameter, the resulting pitch angle is proportional to $\frac{1}{C}$, resulting in a small angle, for which the cosine function is very close to 1 and the sine function is very close to 0: the pitch angle is then considered to be 0° for all springs.

Subsequently, stress analysis is carried out (Figure 3). In particular, the spring is subjected to a shear force and a torsional moment; under large deformations, a bending component also becomes significant.

The maximum shear stress in the wire can be calculated by accounting for the combined effect of shear and torsional loading. The shear stress τ is expressed as:

$$\tau = K_B \frac{8FD}{\pi d^3} \tag{1}$$

where K_B is the Bergstrasser correction factor [46]. The force–displacement relationship under large deformations can be expressed as:

$$\delta = \frac{8FD^3 n}{d^4 cos\alpha_f} \left(\frac{\cos^2 \alpha_f}{G} + \frac{2\sin^2 \alpha_f}{E} \right) \tag{2}$$

With δ being the displacement, E the material Young modulus, and G the material shear modulus. Assuming the material to be isotropic and applying the kinematic relationships illustrated in (Figure 3), one obtains:

$$\delta = \frac{\pi n D_i}{cos(\alpha_i)} (sin\alpha_f - sin\alpha_i) \tag{3}$$

Using Equation (3), the force–deflection angle relationship given in Equation (2) can be reformulated as a direct force–deflection angle relationship, with ν being the material Poisson coefficient:

$$F = \frac{\pi d^4}{8D^2} G \frac{cos^2\alpha_i(sin\alpha_f - sin\alpha_i)}{cos^2\alpha_f(cos^2\alpha_f + \frac{sin^2\alpha_f}{1+\nu})} \tag{4}$$

By substituting F with τ in Equation (4) and expressing it in the form $\tau = G\gamma$, the shear strain γ can be written as:

$$\gamma = \frac{1}{C} \frac{cos^2\alpha_i(sin\alpha_f - sin\alpha_i)}{cos^2\alpha_f(cos^2\alpha_f + \frac{sin^2\alpha_f}{1+\nu})} \tag{5}$$

By employing Brinson's thermomechanical constitutive model [47], it is possible to describe the detwinning process at temperatures below M_S:

$$\tau - \tau_0 = G(\gamma - \gamma_0) + \Omega_\tau(\xi_{S\tau} - \xi_{S\tau 0}) + \frac{\Theta}{\sqrt{3}}(T - T_0) \tag{6}$$

where θ is the thermoelastic coefficient and Ω_τ is the shear transformation constant, expressed as:

$$\Omega_\tau = -\gamma_L G \tag{7}$$

where γ_L is the maximum detwinning shear strain. The term Ω_τ represents the shear stress that compensates for the reduction in stiffness during the detwinning process. The model accounts for the fraction of detwinned martensite through the parameter $\xi_{S\tau}$:

$$\xi_{S\tau} = \frac{1}{2} cos\left(\frac{\pi}{\tau_s^{cr} - \tau_f^{cr}}\left(\tau - \tau_f^{cr}\right)\right) + \frac{1}{2} \tag{8}$$

At low temperatures, stress can be expressed as:

$$\tau = G_M\gamma - G_M\gamma_L\xi_{s\tau} \tag{9}$$

The procedure is subsequently implemented in MATLAB. A force F is assigned, and the corrected maximum stress is computed using Equation (1). The fraction of detwinned martensite is then evaluated using Equation (8), and by inverting Equation (9), the shear strain γ is determined, as shown in Figure 4. At this stage, it is possible to evaluate the final inclination angle of the coil α_f by inverting Equation (4), modified to include the additional term accounting for detwinning:

$$F = \frac{G_M d^4}{8D^3}\left(\pi D \frac{cos^2\alpha_i\left(sin\alpha_f - sin\alpha_i\right)}{cos^2\alpha_{fM}\left(cos^2\alpha_f + \frac{sin^2\alpha_f}{1+\nu}\right)}\right) - \frac{\pi d^3}{8D} G_M\gamma_L\xi_{S\tau} \tag{10}$$

The final elongation can therefore be evaluated as:

$$\delta = \frac{\pi n D}{cos(\alpha_{in})}(sin\alpha_f - sin\,\alpha_{in}) \tag{11}$$

The numerical model served specifically to determine the precise mechanical loads corresponding to 50% and 100% detwinned martensite volume fractions for each spring configuration. The computational framework (Figure 4) calculated the critical force levels required to establish controlled microstructural states prior to rapid thermal actuation testing.

Figure 5 demonstrates the validation of the numerical model against experimental tensile test data for spring-shaped memory alloy specimens. The springs were systematically tested at these predetermined martensite volume fractions, with specific loads reported in Table 3. The load values represent mechanically applied forces necessary to achieve target microstructural conditions before initiating electrothermal activation sequences. This approach ensures reproducible initial conditions for dynamic characterization while eliminating empirical trial-and-error methodologies.

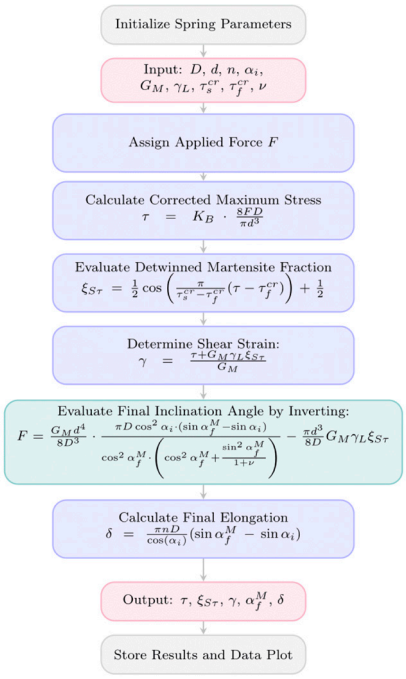


Figure 4. Computational flowchart for MATLAB R2025a implementation.

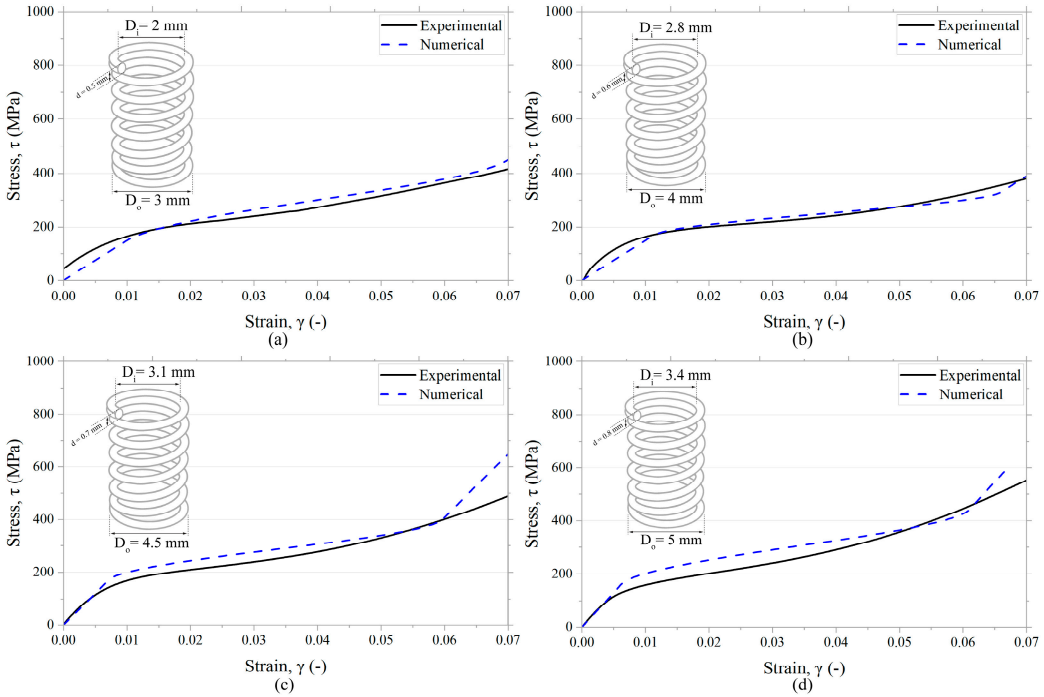


Figure 5. (**a**–**d**) Experimental and numerical shear stress–strain curves for tensile tests on SMA springs specimens for four different geometry types.

Table 3. Applied loads for rapid actuation testing at controlled martensite volume fractions.

Spring Type	Load [N]	% Detwinned Martensite
1 *	3.8	100
2	3.8	50
2	7.2	100
3	3.8	50
3	5.0	100
4	5.0	50
4	7.0	100
5	3.8	50
5	6.0	100
6	3.8	50
6	6.0	100
7	6.0	50
7	8.5	100
8	6.0	50
8	8.5	100
9	7.0	50
9	11.5	100

* Spring Type 1 tested only at 110% detwinning stress (3.8 N) due to experimental constraints; this represents the minimum stable load for the test setup with this wire diameter.

3. Results and Discussion

3.1. Constant Stress Recovery Static Behavior

The temperature–displacement relationships for all springs under various loading conditions (Figure 6) reveal distinct activation characteristics that demonstrate clear load-dependent thermomechanical behavior patterns. The tests have been carried out on the test setup shown in Figure 2, with various constant load conditions and providing slow heating to the SMA actuator through a low electrical current.

The systematic characterization demonstrates three distinct operational domains: low load conditions (3.8–4 N) achieve complete recovery at temperatures of 80–100 °C, indicating minimal stress-induced elevation of transformation temperatures; medium load conditions (6–8.5 N) require temperatures of 100–120 °C, demonstrating progressive stress–temperature coupling effects; and high load conditions (>10 N) necessitate temperatures exceeding 140 °C for full activation, reflecting significant stress-induced transformation temperature increases.

The recovery displacement values span from approximately 20% to over 700%. Here, recovery displacement (%) is computed as $\Delta L/L_0 \times 100$, where L_0 is the initial free length under the given preload. The wide range reflects the combined effect of load level, wire diameter, and spring index on the attainable stroke: lower loads and intermediate spring indices ($C \approx 6.5$–7.5) enable larger recoveries, while higher loads raise transformation temperatures and can limit stroke. This point is critical for applications: high-stroke use cases (e.g., large aperture changes or compliant mechanisms) benefit from settings that favor > 500% recovery, while precision or high-force applications may target lower recoveries to limit thermal and functional fatigue.

The observed relationship between applied stress and recovery displacement reflects the fundamental thermodynamics of stress-induced martensitic transformation. According to the Clausius–Clapeyron relationship, applied stress σ shifts transformation temperatures as $dT/d\sigma \approx -\varepsilon_0 T_0/\Delta H$, where ε_0 is transformation strain, T_0 is transformation temperature, and ΔH is transformation enthalpy. Higher loads therefore require elevated temperatures for complete phase transformation, explaining the reduced recovery displacement ob-

served at higher detwinning stress compared to lower load levels. This stress–temperature coupling is critical for applications requiring predictable force–stroke characteristics.

Figure 7 demonstrates these fundamental thermodynamic relationships governing martensitic transformations in NiTi shape memory alloy springs under applied mechanical loading. The experimental data reveals linear correlations between applied equivalent stress and transformation temperatures, consistent with the Clausius–Clapeyron relationship.

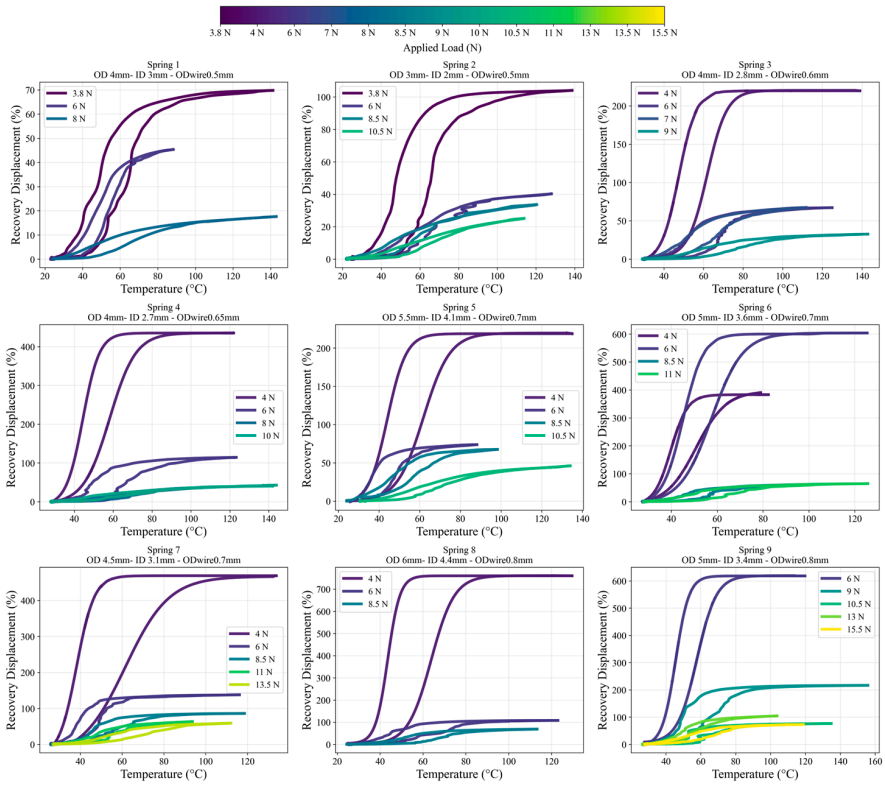


Figure 6. Temperature versus recovery displacement relationships for all SMA springs under different loading conditions.

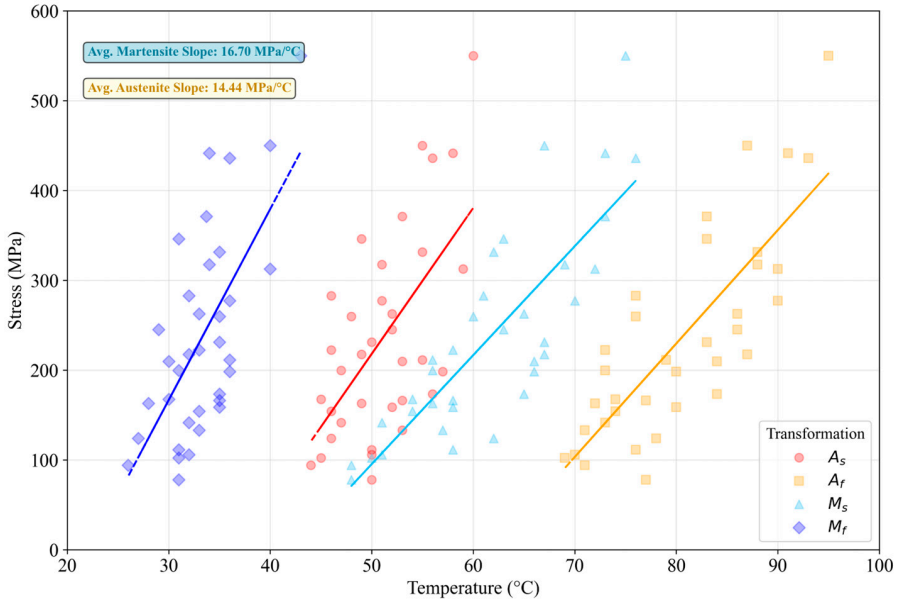


Figure 7. Equivalent stress–temperature phase diagram for shape memory alloy transformations showing austenite (A_s, A_f) and martensite (M_s, M_f) apparent transformation boundaries with slopes of 14.44 and 16.70 MPa/°C, respectively.

The quantitative analysis yields critical design parameters: austenite transformation boundaries (A_s, A_f) exhibit an average slope of 14.44 MPa/°C, while martensite boundaries (M_s, M_f) demonstrate a steeper slope of 16.70 MPa/°C. This differential indicates that martensite formation exhibits greater sensitivity to equivalent stress-induced temperature modifications compared to austenite reversion processes.

The characterization encompasses transformation temperatures from 20 °C to 100 °C under stress levels extending to 600 MPa, establishing comprehensive operational boundaries for engineering applications.

The experimental data confirms that progressively higher loads systematically shift the required activation temperatures toward elevated values due to stress-induced transformation temperature modifications. This phenomenon aligns precisely with fundamental thermodynamic principles governing martensitic transformations, particularly the Clausius–Clapeyron relationship [1]. Recovery displacement percentages varied significantly with applied load levels. Springs tested at 50% martensite detwinning achieved near-complete recovery (95%), while those tested at 100% detwinning showed recovery rates of 80–90%, indicating some residual plastic deformation at higher strain levels.

3.2. Constant Stress Recovery—Dynamic Actuation Performance

The experimental data obtained from rapid actuations was systematically analyzed to generate comprehensive temporal profiles including displacement–time, temperature–time, and current–time traces for each applied current level. For each spring type, tests have been carried out at two different load states as shown in Table 3, providing to the SMA actuator electrical current impulses of predetermined width and length. For each spring geometry and load condition, systematic fast actuation tests were conducted by varying current pulse parameters within a predefined safe operational envelope. The holding time t_m was varied between 0.2 s and 2.0 s in increments of 0.2 s, while current amplitude I ranged from 5 A to 11 A in steps of 1 A. Representative graphical examples of these temporal characteristics are presented in Figure 8a,b. The upper temperature limit of 160 °C was established as a thermal safety constraint to prevent microstructural degradation of the NiTi alloy and ensure stable transformation characteristics over extended operational cycling [1]. This systematic parametric exploration generated the comprehensive actuation performance maps presented in Figures 9 and 10, enabling direct identification of optimal current–duration combinations for specified activation time requirements while maintaining material integrity.

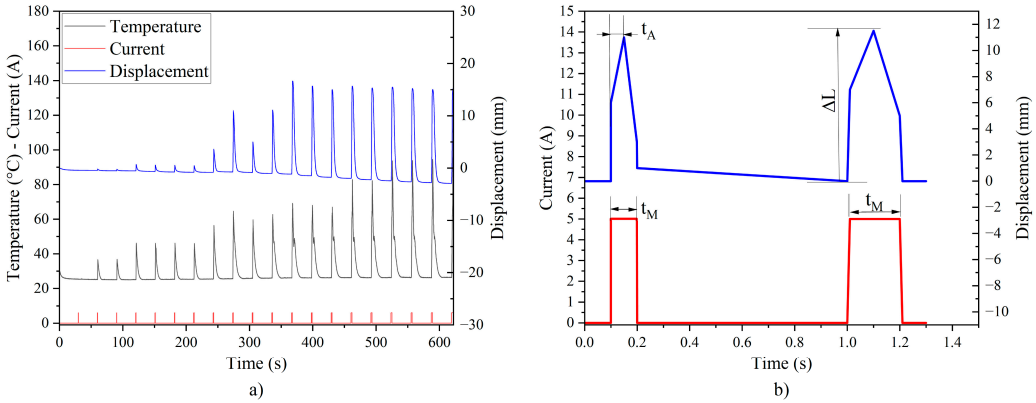


Figure 8. Temporal characterization of SMA spring activation: (**a**) complete activation sequence showing temperature, current, and displacement evolution over extended time periods; (**b**) detailed view of individual activation cycles highlighting holding time (t_M) and activation time (t_A) parameters.

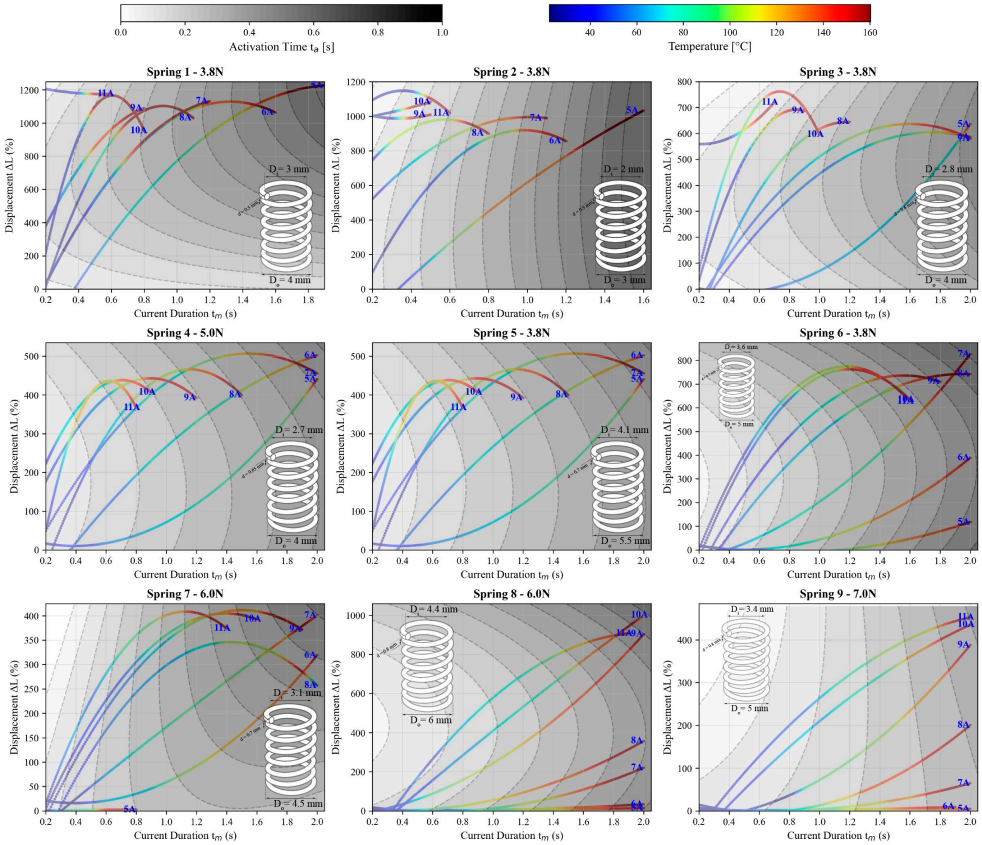


Figure 9. Fast recovery performances for springs 1–9 with loads at 50% detwinned.

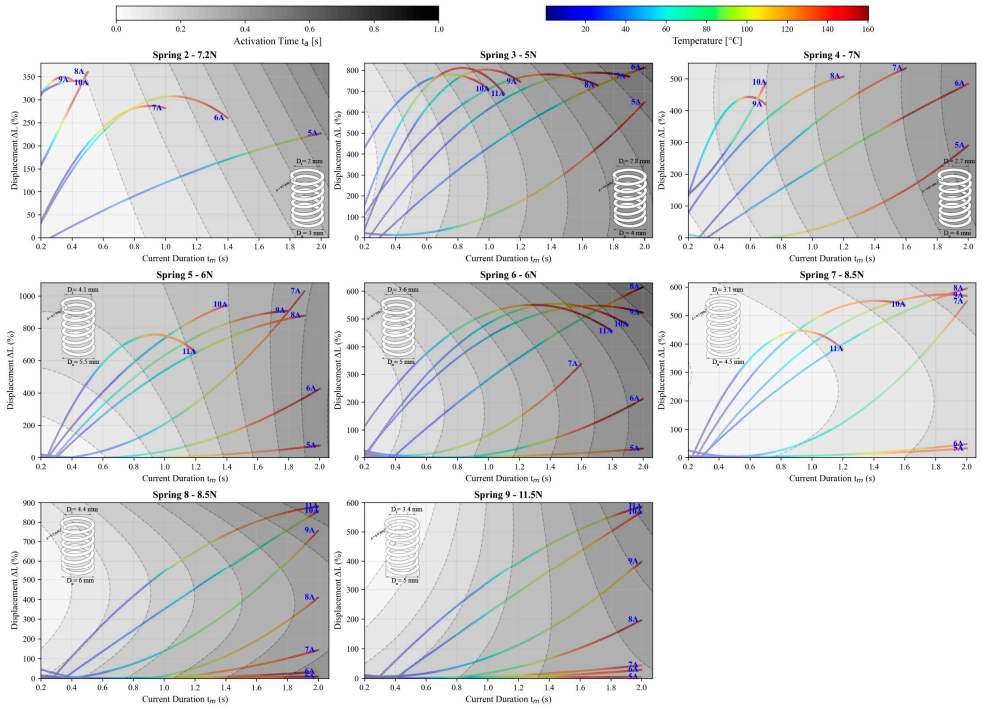


Figure 10. Fast recovery performances for springs 1–9 with loads at 100% detwinned.

Taking the holding time and activation time (t_A), the maximum displacement variation (ΔL) at each activation cycle, and the maximum temperature reached per cycle as primary performance metrics, specialized visualization graphs were developed to provide immediate assessment of the operational zone for each spring configuration at the load levels

specified in Table 3. The performance maps (Figures 9 and 10) present activation time t_a as a function of holding time t_m and current amplitude I. Contour lines represent iso-temporal curves generated through cubic interpolation of experimental data points, enabling rapid identification of optimal current pulse parameters for specified activation times.

These performance mapping visualizations, exemplified in Figures 9 and 10, present the ΔL–t_M relationship with a temperature-based color scale overlay and activation time contour lines for each amplitude of electric current adopted. Figures 9 and 10 serve as design tools enabling rapid selection of actuation parameters. For example, if a target activation time t_a = 1.0 s is required: (1) locate the t_a = 1.0 s contour line, (2) select a point on this contour (e.g., I = 9 A, t_m = 0.8 s), (3) verify the corresponding load capacity meets application requirements. Multiple parameter combinations yield equivalent activation times, allowing optimization for power consumption, thermal management, or cyclic frequency constraints. The contour density indicates sensitivity: closely spaced contours indicate regions where small parameter changes significantly affect activation time, requiring tighter control tolerances. This multi-parameter representation enables rapid identification of optimal operating conditions while simultaneously displaying thermal and temporal constraints for each spring geometry under specified loading conditions. The systematic approach to performance visualization facilitates comprehensive understanding of the electro-thermo-mechanical coupling phenomena inherent in SMA actuator systems, providing essential design guidelines for application-specific optimization strategies.

Key findings from the rapid activation testing include optimal current levels of 5–7 A for thin wires (0.5–0.6 mm) and 8–11 A for thick wires (0.7–0.8 mm), sub-second activation (<1 s) achievable for current durations $\geq$ 0.6 s at optimal current levels, and peak temperatures of 120–160 °C observed during rapid activation, requiring consideration of thermal cycling effects. The contour patterns in Figures 9 and 10 reveal an important design trade-off: equivalent activation times can be achieved through either high current-short duration (rapid heating, minimal heat loss) or moderate current-longer duration (slower heating allowing thermal equilibration). The optimal strategy depends on power supply constraints and desired cyclic frequency.

The activation time analysis revealed optimal current levels for each spring configuration. Lower currents (3–4 A) provided insufficient heating for complete activation, while excessive currents ($\geq$11 A) resulted in overshooting and potential thermal damage. The optimal current range of 5–8 A provided rapid, reliable activation while maintaining operational safety margins.

A crucial aspect of this study is the evaluation of results against design requirements. Taking the requirements of an activation time << 1 s and an activation temperature greater than 100 °C in order to fully complete the martensitic transformation, the systematic analysis of the results enables the identification of which springs and current levels meet these operational criteria, as reported in Table 4.

This comprehensive assessment methodology provides essential insights for actuator selection and control parameter optimization. For instance, spring 1 operating under a 3.8 N load demonstrates compliance with the established requirements across multiple current levels (5 A, 6 A, 7 A, 8 A, 9 A, 10 A, and 11 A), indicating robust operational flexibility within the specified parameters. Conversely, higher-capacity springs such as spring 9 require elevated current levels (11.5 A) to achieve the requisite performance thresholds, particularly under increased mechanical loading conditions.

Table 4. Systematic analysis of design requirements compliance for shape memory alloy spring actuators under variable current loading conditions.

Spring Type	Load [N]	5 A	6 A	7 A	8 A	9 A	10 A	11 A
1	3.8		✓	✓	✓	✓	✓	✓
2	3.8	✓	✓	✓	✓	✓	✓	✓
	7.2		✓	✓	✓	✓	✓	✓
3	3.8				✓	✓	✓	✓
	5				✓	✓	✓	✓
4	5			✓	✓	✓	✓	✓
	7				✓	✓	✓	✓
5	3.8				✓	✓	✓	✓
	6						✓	✓
6	3.8					✓	✓	✓
	6							✓
7	6							✓
	8.5							✓
8	6							✓
	8.5							
9	7							✓
	11.5							

The systematic variation in spring geometry reveals important scaling relationships for thermal management. Wire diameter d governs three critical parameters:

1. **Electrical Resistance:** $R \propto 1/d^2$, requiring quadratically higher current for equivalent power input in thinner wires.
2. **Thermal Mass:** Heat capacity $\propto d^2$, meaning thinner wires heat and cool more rapidly.
3. **Surface Area to Volume Ratio:** $(A/V) \propto 1/d$, enhancing convective cooling in thin wires.

These competing effects create an optimal wire diameter for rapid actuation: sufficiently thin to minimize thermal mass, yet thick enough to limit resistive losses and convective cooling. Our results indicate this optimum lies near d = 0.5–0.7 mm for the investigated current range (5–11 A). Spring index C = D/d influences mechanical stress distribution but has secondary effects on thermal response through changes in active wire length. Higher spring indices provide greater stroke but require proportionally more thermal energy for equivalent displacement, explaining the activation time trends observed across different spring geometries.

4. Conclusions

This comprehensive investigation of fast electrical activation in shape memory alloy spring actuators has established fundamental design principles and operational guidelines that significantly advance the field of rapid SMA actuation technology. The systematic experimental characterization of nine different spring configurations, encompassing wire diameters from 0.5 to 0.8 mm and spring indices from 6.0 to 8.0, has revealed critical relationships between geometric parameters, thermal management strategies, and actuator performance that directly influence both immediate response characteristics and long-term operational reliability. The achievement of sub-second activation times while maintaining structural integrity represents a substantial advancement in SMA actuator technology, with profound implications for applications in exoskeletons, medical devices, robotics, and automation systems where rapid, reliable actuation is paramount.

The comprehensive analysis of experimental data revealed several critical insights for SMA spring actuator optimization, providing fundamental design guidelines for enhanced performance and operational longevity. These findings establish key relationships between geometric parameters, material properties, and operational strategies that directly influence actuator effectiveness. The systematic investigation of spring geometry demonstrated that springs with intermediate spring indices (C = 6.5–7.5) provided the optimal balance between force output capability and displacement range characteristics, representing a critical design parameter for maximizing actuator performance while maintaining mechanical reliability. Springs with very low spring indices resulted in excessive stress concentrations that compromised structural integrity, while configurations with high spring indices exhibited reduced force capacity due to geometric constraints. This geometric optimization window establishes a fundamental constraint that must be carefully considered in the design phase to ensure both performance and durability requirements are met.

The analysis revealed distinct performance trade-offs associated with wire diameter selection that have significant implications for application-specific design strategies. Larger wire diameters (0.7–0.8 mm) required elevated activation currents for complete transformation but provided enhanced force output capacity, making them particularly suitable for high-load applications where durability is prioritized over rapid response. Conversely, smaller wire diameters (0.5–0.6 mm) enabled accelerated thermal response characteristics due to reduced thermal mass but exhibited correspondingly reduced load capacity limitations, positioning them as optimal choices for applications requiring rapid actuation with moderate force requirements. This fundamental relationship between wire geometry and thermomechanical performance establishes essential design considerations that must be balanced against specific application requirements to achieve optimal system performance.

The thermal management strategies developed through this research demonstrate that optimal activation protocols involve moderate current levels (5–7 A) with precisely controlled pulse durations to minimize thermal stress accumulation while ensuring complete martensitic transformation. The experimental data demonstrated that rapid heating phases followed by natural cooling cycles provided the optimal balance between activation speed and long-term operational longevity, with this thermal management approach minimizing temperature overshoot effects that can lead to material degradation and preserving the inherent thermomechanical properties of the SMA material system. The identification of optimal current ranges for different wire configurations, 5–7 A for thin wires and 8–11 A for thick wires, provides practical guidelines for system designers, while the observation of peak temperatures reaching 120–160 °C during rapid activation emphasizes the critical importance of thermal cycling considerations in long-term system design.

The characterization results established that operating springs at approximately 50% of maximum detwinning capacity provided optimal performance characteristics with minimal degradation over repeated operational cycles, representing a fundamental operational constraint for maximizing both performance and durability in practical actuator applications. Higher strain levels resulted in accelerated fatigue progression and reduced shape recovery characteristics, while lower strain levels underutilized the material's inherent actuation potential. This operational window provides clear guidance for system designers seeking to balance performance requirements with longevity expectations, ensuring that SMA actuators can deliver consistent performance over extended operational periods.

The achievement of sub-second activation times with displacement recoveries reaching 600–800% strain represents a breakthrough in SMA actuator technology, demonstrating that rapid actuation is achievable without compromising the fundamental advantages of SMA materials. The experimental validation of these performance characteristics under controlled conditions provides confidence in the reproducibility and reliability of these

results across different operating environments. The comprehensive characterization approach, incorporating differential scanning calorimetry, mechanical testing, infrared thermography, and laser displacement sensing, ensures that the findings are based on robust experimental evidence and can be confidently applied to real-world applications.

The implications of this research extend beyond the immediate technical achievements to encompass broader considerations for the integration of SMA actuators into advanced engineering systems. The established design guidelines provide a foundation for developing next-generation actuation systems that can meet the demanding requirements of modern applications while the demonstrated performance characteristics open new possibilities for applications previously considered unsuitable for SMA technology due to speed limitations. The combination of rapid response and high force output positions these optimized SMA spring actuators as viable alternatives to conventional actuation technologies in applications where their unique advantages can be fully exploited.

Author Contributions: Conceptualization, S.R. and C.M.; Data curation, S.R., M.C. and C.M.; Formal analysis, S.R., M.C., A.C. and G.R.; Funding acquisition, C.M.; Investigation, S.R., M.C., A.C. and G.R.; Methodology, S.R., M.C., A.C. and G.R.; Project administration, C.M.; Resources, C.M.; Software, S.R., M.C., A.C. and G.R.; Supervision, C.M.; Validation, S.R., M.C., A.C. and G.R.; Visualization, S.R.; Writing—original draft, S.R. and A.C.; Writing—review and editing, C.M. All authors have read and agreed to the published version of the manuscript.

Funding: This research was funded by the Italian Ministry of University and Research (MUR), grant number PE00000015. The APC was funded by the Italian Ministry of University and Research (MUR) through the National Recovery and Resilience Plan (PNRR), Mission 4, Component 2, Project AGE-IT (PE00000015).

Institutional Review Board Statement: Not applicable.

Informed Consent Statement: Not applicable.

Data Availability Statement: The data that supports the findings of this study is not publicly available.

Acknowledgments: This research was conducted within the framework of the CASCADE Program pursuant to Ministerial Decree D.D. 343/2024 dated 29 February 2024, issued by the University of Florence for the submission of research proposals developed by Research Organizations and Enterprises under the research program "AGE-IT—AGEING WELL IN AN AGEING SOCIETY." Spoke 9. The authors gratefully acknowledge the financial support provided through the National Recovery and Resilience Plan (PNRR), Mission 4 "Education and Research"—Component 2 Project Code PE00000015, CUP B83C22004800006.

Conflicts of Interest: Authors Matteo Chiodo, Antonio Corigliano and Giuseppe Rota were employed by the company 2SMArtEST. The remaining authors declare that the research was conducted in the absence of any commercial or financial relationships that could be construed as a potential conflict of interest.

References

1. Lagoudas, D.C. *Shape Memory Alloys: Modeling and Engineering Applications*; Springer: New York, NY, USA, 2008.
2. Otsuka, L.; Wayman, C.M. *Shape Memory Materials*; Cambridge University Press: Cambridge, UK, 1998.
3. Giovinco, V.; Kotak, P.; Cichella, V.; Maletta, C.; Lamuta, C. Dynamic model for the tensile actuation of thermally and electrothermally actuated twisted and coiled artificial muscles (TCAMs). *Smart Mater. Struct.* **2020**, *29*, 025004. [CrossRef]
4. Mohd Jani, J.; Leary, M.; Subic, A.; Gibson, M.A. A review of shape memory alloy research, applications and opportunities. *Mater. Des.* **2014**, *56*, 1078–1113. [CrossRef]
5. Hartl, D.J.; Lagoudas, D.C. Aerospace applications of shape memory alloys. *Proc. Inst. Mech. Eng. Part G J. Aerosp. Eng.* **2007**, *221*, 535–552. [CrossRef]
6. Sun, Q.P.; Hwang, K.C. Micromechanics modelling for the constitutive behavior of polycrystalline shape memory alloys—I. Derivation of general relations. *J. Mech. Phys. Solids* **1993**, *41*, 1–17. [CrossRef]

7. Nemov, A.; Saren, A. 3-D Meso-Scale Finite Element Calculations of Free Energy on Twin Boundaries in Magnetic Shape Memory Alloys. *IEEE Trans. Magn.* **2024**, *60*, 2000712. [CrossRef]
8. Cisse, C.; Zaki, W.; Ben Zineb, T. A review of constitutive models and modeling techniques for shape memory alloys. *Int. J. Plast.* **2016**, *76*, 244–284. [CrossRef]
9. Sgambitterra, E.; Maletta, C.; Furgiuele, F. Investigation on Crack Tip Transformation in NiTi Alloys: Effect of the Temperature. *Shape Mem. Superelasticity* **2015**, *1*, 275–283. [CrossRef]
10. Barbarino, S.; Flores, E.S.; Ajaj, R.M.; Friswell, M.I.; Dayyani, I. A review on shape memory alloys with applications to morphing aircraft. *Smart Mater. Struct.* **2014**, *23*, 063001. [CrossRef]
11. Huang, W. On the selection of shape memory alloys for actuators. *Mater. Des.* **2002**, *23*, 11–19. [CrossRef]
12. Sgambitterra, E.; Maletta, C.; Furgiuele, F. Modeling and simulation of the thermo-mechanical response of NiTi-based Belleville springs. *J. Intell. Mater. Syst. Struct.* **2016**, *27*, 81–91. [CrossRef]
13. Elahinia, M.H.; Hashemi, M.; Tabesh, M.; Borghesani, S.B. Manufacturing and processing of NiTi implants: A review. *Prog. Mater. Sci.* **2012**, *57*, 911–946. [CrossRef]
14. Jani, J.M.; Huang, S.; Leary, M. Numerical modeling of shape memory alloy linear actuator. *Comput. Mech.* **2014**, *53*, 1079–1094. [CrossRef]
15. Andianesis, K.; Tzes, A. Design of an anthropomorphic prosthetic hand driven by Shape Memory Alloy actuators. In Proceedings of the 2008 2nd IEEE RAS & EMBS International Conference on Biomedical Robotics and Biomechatronics, Scottsdale, AZ, USA, 19–22 October 2008; pp. 1–6. [CrossRef]
16. Hamid, Q.A.; Wan Hasan, W.Z.; Azmah Hanim, M.A.; Nuraini, A.A.; Hamidon, M.N.; Ramli, H.R. Shape memory alloys actuated upper limb devices: A review. *Sens. Actuators Rep.* **2023**, *5*, 100160. [CrossRef]
17. Duerig, T.; Pelton, A.; Stöckel, D. An overview of nitinol medical applications. *Mater. Sci. Eng. A* **1999**, *273*, 149–160. [CrossRef]
18. Lecce, L.; Concilio, A. *Shape Memory Alloy Engineering: For Aerospace, Structural and Biomedical Applications*; Butterworth-Heinemann: Oxford, UK, 2015.
19. Mansilla Navarro, P.; Copaci, D.; Arias, J.; Blanc Rojas, D. Design of an SMA-Based Actuator for Replicating Normal Gait Patterns in Pediatric Patients with Cerebral Palsy. *Biometrics* **2024**, *9*, 376. [CrossRef]
20. Lu, L.; Cui, J.; Nawarathne, D.D. Magnetic Field Sensing with Magnetic Shape Memory Alloy and Fiber Bragg Grating on Silica and Polymer Optical Fibers. *IEEE Trans. Instrum. Meas.* **2025**, *74*, 7007008. [CrossRef]
21. Rodinò, S.; Curcio, E.M.; Sgambitterra, E.; Maletta, C. SMA-Polymer Composite Made by 3D Printing: Modelling and Experiments. *Procedia Struct. Integr.* **2023**, *47*, 579–588. [CrossRef]
22. Kim, M.S. Shape Memory Alloy (SMA) Actuators: The Role of Material, Form, and Scaling Effects. *Adv. Mater.* **2023**, *35*, e2208517. [CrossRef] [PubMed]
23. Rao, A.; Srinivasa, A.R.; Reddy, J.N. *Design of Shape Memory Alloy (SMA) Actuators*, 1st ed.; Springer: Cham, Switzerland, 2015. [CrossRef]
24. Leal, M.L.; Pino, L.; Barati, M.; Saint-Sulpice, L.; Daniel, L.; Chirani, S.A. Modeling of functional fatigue of SMA-based actuators under thermomechanical loading and Joule heating. *Int. J. Fatigue* **2024**, *179*, 108055. [CrossRef]
25. Delpueyo, D.; Balandraud, X.; Grédiac, M. Applying full-field measurement techniques for the thermomechanical characterization of shape memory alloys. *Smart Mater. Struct.* **2020**, *8*, 29. [CrossRef]
26. Yu, Y.; Nie, L.; Zhang, X. Finite-Iteration Learning Tracking Control of Magnetic Shape Memory Alloy Actuator Based on Neural Network. *IEEE Trans. Circuits Syst. II Express Briefs* **2025**. [CrossRef]
27. Bhatt, N.; Soni, S.; Singla, A. Analyzing the effect of parametric variations on the performance of antagonistic SMA spring actuator. *Mater. Today Proc.* **2022**, *31*, 103728. [CrossRef]
28. Yi, H. Simulation of Shape Memory Alloy (SMA)-Bias Spring Actuation for Self-Shaping Architecture. *Materials* **2020**, *13*, 2485. [CrossRef]
29. Rodinò, S.; Caroleo, G.; Sgambitterra, E.; Bruno, F.; Muzzupappa, M.; Maletta, C. A multiphysics dynamic model for shape memory alloy actuators. *Sens. Actuators Phys.* **2023**, *362*, 114602. [CrossRef]
30. Sgambitterra, E.; Greco, C.; Rodinò, S.; Niccoli, F.; Furgiuele, F.; Maletta, C. Fully coupled electric-thermo-mechanical model for predicting the response of a SMA wire activated by electrical input. *Sens. Actuators Phys.* **2023**, *362*, 114643. [CrossRef]
31. Karunakaran, S.; Abang Haji Abdul Majid, D.L.; Jaafar, C.; Ismail, M.; Yahya, H. Heating Techniques of Shape Memory Alloy (SMA)—A Review. *J. Adv. Res. Fluid Mech. Therm. Sci.* **2022**, *78*, 78–90. [CrossRef]
32. Neugebauer, R.; Bucht, A.; Pagel, K.; Jung, J. *Numerical Simulation of the Activation Behavior of Thermal Shape Memory Alloys*; Fraunhofer IWU: Chemnitz, Germany, 2008.
33. Shayanfard, P.; Kadkhodaei, M.; Jalalpour, A. Numerical and Experimental Investigation on Electro-Thermo-Mechanical Behavior of NiTi Shape Memory Alloy Wires. *Iran. J. Sci. Technol. Trans. Mech. Eng.* **2019**, *43*, 621–629. [CrossRef]
34. Vollach, S.; Shilo, D. The Mechanical Response of Shape Memory Alloys Under a Rapid Heating Pulse. *Exp. Mech.* **2010**, *50*, 803–811. [CrossRef]

35. Vollach, S.; Shilo, D.; Shlagman, H. Mechanical Response of Shape Memory Alloys Under a Rapid Heating Pulse—Part II. *Exp. Mech.* **2016**, *56*, 1465–1475. [CrossRef]
36. Motzki, P.; Gorges, T.; Kappel, M.; Schmidt, M.; Rizzello, G.; Seelecke, S. High-Speed and High-Efficiency Shape Memory Alloy Actuation. *Smart Mater. Struct.* **2018**, *27*, 075047. [CrossRef]
37. Dana, A.; Vollach, S.; Shilo, D. Use the Force: Review of High-Rate Actuation of Shape Memory Alloys. *Actuators* **2021**, *10*, 140. [CrossRef]
38. Zhang, Y.; Zhang, X.; Jiang, J.; Zhang, Q.; Ke, Y.; Qiu, S. Actuation response of typical biased shape memory alloy wire under variable electric heating rates: Experimental investigation and modeling. *J. Intell. Mater. Syst. Struct.* **2022**, *33*, 2258–2275. [CrossRef]
39. Talebi, H.; Golestanian, H.; Zakerzadeh, M.R.; Homaei, H. Thermoelectric heat transfer modeling of shape memory alloy actuators. In Proceedings of the 22st Annual International Conference on Mechanical Engineering-ISME2014, Ahvaz, Iran, 22 April 2014.
40. Nizamani, A.M.; Daudpoto, J.; Nizaman, M.A. *Development of Faster SMA Actuators*; InTech Open: London, UK, 2018.
41. Motzki, P. Efficient SMA Actuation—Design and Control Concepts. *Proceedings* **2020**, *64*, 20. [CrossRef]
42. Wang, Z.; Zu, X.; Feng, X.; Dai, J. Effect of thermomechanical treatment on the two-way shape memory effect of NiTi alloy spring. *Mater. Lett.* **2002**, *54*, 55–61. [CrossRef]
43. Wang, Z.G.; Zu, X.T.; Feng, X.D.; Zhu, S.; Deng, J.; Wang, L.M. Effect of electrothermal annealing on the transformation behavior of TiNi shape memory alloy and two-way shape memory spring actuated by direct electrical current. *Phys. B* **2004**, *349*, 365–370. [CrossRef]
44. Wang, Z.G.; Zu, X.T.; Feng, X.D.; Zhu, S.; Bao, J.W.; Wang, L.M. Characteristics of two-way shape memory TiNi springs driven by electrical current. *Mater. Des.* **2004**, *25*, 699–703. [CrossRef]
45. An, S.M.; Ryu, J.; Cho, M.; Cho, K.J. Engineering design framework for a shape memory alloy coil spring actuator using a static two-state model. *Smart Mater. Struct.* **2012**, *21*, 055009. [CrossRef]
46. Richard, G.B.; Keith, N.J. *Shigley: Progetto e Costruzione di Macchine*; McGraw-Hill Education: New York, NY, USA, 2018.
47. Brinson, L.C. One-dimensional constitutive behavior of shape memory alloys: Thermomechanical derivation with non-constant material functions and redefined martensite internal variable. *J. Intell. Mater. Syst. Struct.* **1993**, *4*, 229–242. [CrossRef]

Disclaimer/Publisher's Note: The statements, opinions and data contained in all publications are solely those of the individual author(s) and contributor(s) and not of MDPI and/or the editor(s). MDPI and/or the editor(s) disclaim responsibility for any injury to people or property resulting from any ideas, methods, instructions or products referred to in the content.